Non-contact time-resolved diffuse reflectance imaging at null source-detector separation

M. Mazurenka,[1,*] A. Jelzow,[1] H. Wabnitz,[1] D. Contini,[2] L. Spinelli,[3] A. Pifferi,[2,3,4] R. Cubeddu,[2,3,4] A. Dalla Mora,[2] A. Tosi,[5] F. Zappa,[5,6] and R. Macdonald[1]

[1]*Physikalisch-Technische Bundesanstalt, Abbestr. 2-12, 10587, Berlin, Germany*
[2]*Dipartimento di Fisica, Politecnico di Milano, Piazza Leonardo da Vinci 32, Milano I-20133, Italy*
[3]*Istituto di Fotonica e Nanotecnologie, Consiglio Nazionale delle Ricerche, Piazza Leonardo da Vinci 32, Milano I-20133, Italy*
[4]*IIT Res. Unit, Politecnico di Milano, Piazza Leonardo da Vinci 32, Milano I-20133, Italy*
[5]*Dipartimento di Elettronica e Informazione, Politecnico di Milano, Piazza Leonardo da Vinci 32, Milano I-20133, Italy*
[6]*Micro Photon Devices Srl, Via Stradivari 4, Bolzano I-39100, Italy*
[*]*mikhail.mazurenka@ptb.de*

Abstract: We report results of the proof-of-principle tests of a novel non-contact tissue imaging system. The system utilizes a quasi-null source-detector separation approach for time-domain near-infrared spectroscopy, taking advantage of an innovative state-of-the-art fast-gated single photon counting detector. Measurements on phantoms demonstrate the feasibility of the non-contact approach for the detection of optically absorbing perturbations buried up to a few centimeters beneath the surface of a tissue-like turbid medium. The measured depth sensitivity and spatial resolution of the new system are close to the values predicted by Monte Carlo simulations for the inhomogeneous medium and an ideal fast-gated detector, thus proving the feasibility of the non-contact approach for high density diffuse reflectance measurements on tissue. Potential applications of the system are also discussed.

References and links

1. M. Wolf, M. Ferrari, and V. Quaresima, "Progress of near-infrared spectroscopy and topography for brain and muscle clinical applications," J. Biomed. Opt. **12**(6), 062104 (2007).
2. J. Steinbrink, H. Wabnitz, H. Obrig, A. Villringer, and H. Rinneberg, "Determining changes in NIR absorption using a layered model of the human head," Phys. Med. Biol. **46**(3), 879–896 (2001).
3. A. Liebert, H. Wabnitz, J. Steinbrink, H. Obrig, M. Möller, R. Macdonald, A. Villringer, and H. Rinneberg, "Time-resolved multidistance near-infrared spectroscopy of the adult head: intracerebral and extracerebral absorption changes from moments of distribution of times of flight of photons," Appl. Opt. **43**(15), 3037–3047 (2004).
4. H. Wabnitz, M. Möller, A. Liebert, A. Walter, R. Macdonald, H. Obrig, J. Steinbrink, R. Erdmann, and O. Raitza, "A time-domain NIR brain imager applied in functional stimulation experiments," Proc. SPIE **5859**, 58590H (2005).
5. T. H. Sander, A. Liebert, B. M. Mackert, H. Wabnitz, S. Leistner, G. Curio, M. Burghoff, R. Macdonald, and L. Trahms, "DC-magnetoencephalography and time-resolved near-infrared spectroscopy combined to study neuronal and vascular brain responses," Physiol. Meas. **28**(6), 651–664 (2007).
6. M. Butti, D. Contini, E. Molteni, M. Caffini, L. Spinelli, G. Baselli, A. M. Bianchi, S. Cerutti, R. Cubeddu, and A. Torricelli, "Effect of prolonged stimulation on cerebral hemodynamic: a time-resolved fNIRS study," Med. Phys. **36**(9), 4103–4114 (2009).
7. A. Pifferi, A. Torricelli, L. Spinelli, D. Contini, R. Cubeddu, F. Martelli, G. Zaccanti, A. Tosi, A. Dalla Mora, F. Zappa, and S. Cova, "Time-resolved diffuse reflectance using small source-detector separation and fast single-photon gating," Phys. Rev. Lett. **100**(13), 138101 (2008).
8. A. Dalla Mora, A. Tosi, F. Zappa, S. Cova, D. Contini, A. Pifferi, L. Spinelli, A. Torricelli, and R. Cubeddu, "Fast-gated single-photon avalanche diode for wide dynamic range near infrared spectroscopy," IEEE J. Sel.

Top. Quantum Electron. **16**(4), 1023–1030 (2010).
9. A. Tosi, A. D. Mora, F. Zappa, A. Gulinatti, D. Contini, A. Pifferi, L. Spinelli, A. Torricelli, and R. Cubeddu, "Fast-gated single-photon counting technique widens dynamic range and speeds up acquisition time in time-resolved measurements," Opt. Express **19**(11), 10735–10746 (2011).
10. A. Torricelli, A. Pifferi, L. Spinelli, R. Cubeddu, F. Martelli, S. Del Bianco, and G. Zaccanti, "Time-resolved reflectance at null source-detector separation: improving contrast and resolution in diffuse optical imaging," Phys. Rev. Lett. **95**(7), 078101 (2005).
11. L. Spinelli, F. Martelli, S. Del Bianco, A. Pifferi, A. Torricelli, R. Cubeddu, and G. Zaccanti, "Absorption and scattering perturbations in homogeneous and layered diffusive media probed by time-resolved reflectance at null source-detector separation," Phys. Rev. E Stat. Nonlin. Soft Matter Phys. **74**(2), 021919 (2006).
12. A. Kienle, L. Lilge, M. S. Patterson, R. Hibst, R. Steiner, and B. C. Wilson, "Spatially resolved absolute diffuse reflectance measurements for noninvasive determination of the optical scattering and absorption coefficients of biological tissue," Appl. Opt. **35**(13), 2304–2314 (1996).
13. T. Funane, H. Atsumori, A. Suzuki, and M. Kiguchi, "Noncontact brain activity measurement system based on near-infrared spectroscopy," Appl. Phys. Lett. **96**(12), 123701 (2010).
14. X. Wang, Z. Zhao, W. Becker, T. Troxler, and B. Chance, "Flying spot remote sensing of ICG kinetics of undeformed tissues," Proc. SPIE **5693**, 28–33 (2005).
15. I. Sase, A. Takatsuki, J. Seki, T. Yanagida, and A. Seiyama, "Noncontact backscatter-mode near-infrared time-resolved imaging system: Preliminary study for functional brain mapping," J. Biomed. Opt. **11**(5), 054006 (2006).
16. V. Sankaran, J. T. Walsh, Jr., and D. J. Maitland, "Comparative study of polarized light propagation in biologic tissues," J. Biomed. Opt. **7**(3), 300–306 (2002).
17. F. Martelli and G. Zaccanti, "Calibration of scattering and absorption properties of a liquid diffusive medium at NIR wavelengths. CW method," Opt. Express **15**(2), 486–500 (2007).
18. Q. Zhao, L. Spinelli, A. Bassi, G. Valentini, D. Contini, A. Torricelli, R. Cubeddu, G. Zaccanti, F. Martelli, and A. Pifferi, "Functional tomography using a time-gated ICCD camera," Biomed. Opt. Express **2**(3), 705–716 (2011).

1. Introduction

Over the past three decades, near-infrared spectroscopy (NIRS) has evolved as a powerful research and diagnostics tool for both laboratory studies and clinical trials. A plethora of studies on various applications, including measurements of oxygen consumption of muscle, tissue oximetry, monitoring of cerebral blood flow, and functional brain mapping have been reported and are summarized in [1]. The non-invasive nature and wide applicability of NIRS methods as well as the relatively low costs of devices compared to other modalities for functional imaging and diagnosis triggered the evolution of several distinct approaches: continuous wave (cw) NIRS, spatially resolved (sr), time-resolved (tr) and phase modulation (pm) NIRS. For the field of the functional activation of human cerebral cortex trNIRS is one of the most promising techniques [2–6] despite several existing drawbacks, such as imprecise anatomical localization, sensor-tissue contact problems, low depth localization and poor lateral spatial resolution.

Recent development of fast-gated Single-Photon Avalanche Diode (SPAD) detectors [7–9] opened up new perspectives for trNIRS by introduction of a novel measurement method, *i.e.* the Null Source-Detector Separation (NSDS) approach [7,10]. The method is based on the detection of trNIRS diffuse reflectance signals at the point of light insertion into the tissue, contrary to the classical NIRS, where source-detector separations of 20 mm to 40 mm are commonly used. The decrease of the source-detector separation in the NSDS approach results in an enormous increase in the number of the early photons (up to four orders of magnitude) [10]. However, these photons do not carry information about deeper layers of the tissue and are discarded in NSDS by a fast-gated SPAD, which is photosensitive during the gate-on window only (late only photons detection). The following advantages of the NSDS approach over classical trNIRS have been shown theoretically: (*i*) the absolute number of photons detected at any time at null-distance is larger than in conventional trNIRS, (*ii*) NSDS measurements exhibit better or comparable contrast and spatial resolution compared to larger source-detector separations for an *absorbing* inclusion at any depth, and for *any* time after light injection, (*iii*) for a *scattering* inclusion, both contrasts are comparable at late times

[10,11]. Furthermore, the feasibility of this approach using a fast-gated SPAD was also demonstrated experimentally [7].

In this paper we report on a proof-of-concept test of a novel non-contact time-domain brain imaging system, designed to implement the recently developed NSDS-NIRS together with fast-gated SPAD detection. The non-contact design is intended to avoid many issues attributed to sensor-tissue contact like e.g. skin compression, local blood content alterations, and to obtain a reduction in measurement preparation time and an increase in comfort for the subjects (in particular for sleep studies) [12,13]. Null or quasi-null source-detector imaging, in turn, will provide better localization of cerebral cortex activations or defects by providing a dense, flexible grid of measurement points and is envisaged to be also helpful in tracking the object during the untethered movements of the head, in the case of functional brain mapping, or limbs, chest, breast in other NIRS applications [14,15]. However, the applicability of the designed scanning imager is limited to application on hairless parts of the head, such as the forehead, or other tissues of hairless body parts like muscles or breast.

2. Experimental setup

As the first stage of the development, a device for single point measurements (with no optical scanning elements) has been designed and built to perform the proof-of-concept tests.

Radiation from a supercontinuum laser (Fianium Ltd., UK, repetition rate 20 MHz, pulse duration <100 ps) coupled to an acousto-optical tunable filter (AOTF, NEOS Technologies, USA, $\Delta\lambda$ = 1 nm), tuned to a wavelength of 690 nm, was used as a light source. The optical system was built in a confocal configuration. In our reflectance measurements the photons diffusively scattered by the medium under investigations are of the same energy as the incident photons (shown in different colors in Fig. 1 only for the purpose to distinguish incident and detected photons pathways) and, therefore, should propagate back along the path of the incident photons, i.e. back to the laser system. To detect diffusively scattered photons as well as to suppress the directly reflected or minimally scattered photons we implemented a polarization selective detection, despite its ~50% signal loss. It consists of a polarizer P (Thorlabs Inc., USA) and a polarizing cube beamsplitter, PBS (CVI Melles Griot, USA), see Fig. 1. The polarizer serves to clean up the linear polarization of the incident light after the AOTF. The polarizing cube beamsplitter is aligned to reflect the linearly polarized light coming from the AOTF and the polarizer to a pair of image transfer lenses (Ø 25,4 mm, f = 100 mm and f = 150 mm, AR coated, Thorlabs Inc., USA), with focus on the surface of the sample.

Light scattered by turbid media or biological tissues is randomly polarized [16]. Thus, half of it, polarized perpendicularly to the incident light, passes through the polarizing cube beamsplitter and can be detected by our state-of-the-art gated SPAD (provided by Micro Photon Devices Srl, Italy) which has a 100 µm diameter sensitive area. The resulting distributions of time of flight (DTOFs) of the photons were recorded by a time-correlated single photon counting card (SPC-134, Becker & Hickl GmbH, Germany).

The optical system was aligned in a way that the incident and detection points were slightly (~1 mm, see inset in Fig. 1) apart from each other, rather than for a real NSDS. This was done to avoid direct multiple reflections from the fiber coupler lens and the surface of the polarizing cube beamsplitter, which gave well detectable signals despite broadband AR coatings on both the lens and the beamsplitter. The whole optical system was assembled in a rigid cage system (Thorlabs Inc., USA) and the alignment was done by slightly tilting the mirror M (Fig. 1). The magnitude of separation between source and detection point was controlled by connecting a laser light source to the detection fiber and tracing the light path back to the phantom. It should be noted, however, that the real null-distance alignment can as well be realized with our set-up by using optimized custom optics, such as custom narrow-band anti-reflection coatings on all optics (as narrow-band AR coatings perform better than

broadband used in this experiment), custom made polarization splitting plate instead of the cube, etc.
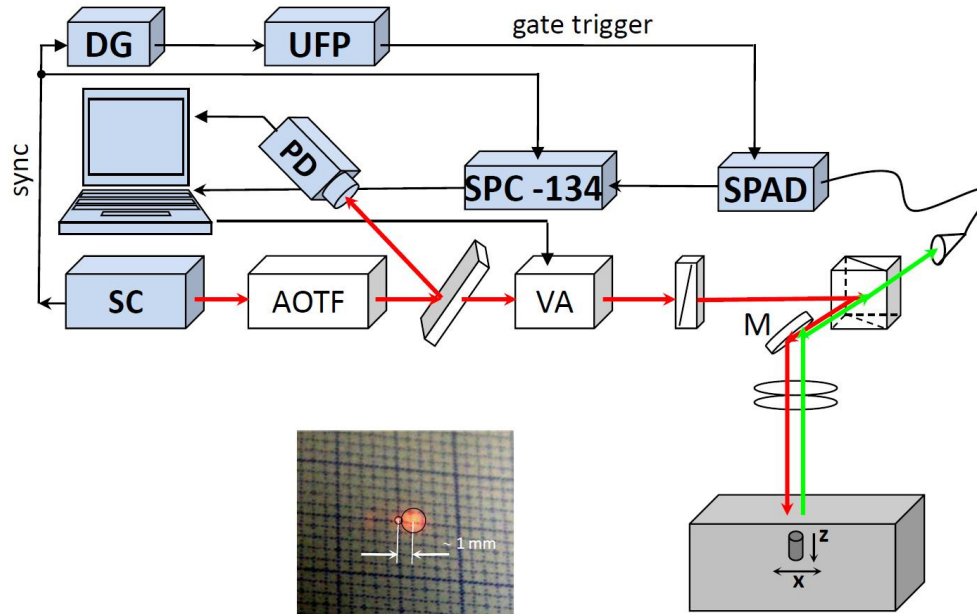

Fig. 1. Schematic of the non-contact brain scanning imaging system. Red lines show the incident light pathway, green – the collected light pathway. Black lines represent electrical connections. The inset shows the alignment of the system: the focused spot on the left is the laser light incident point; the larger diffuse spot 1 mm to the right is the detection area. (SC – supercontinuum laser; VA – variable attenuator; PD – photodiode; DG – delay generator; UFP – ultrafast pulser; M – mirror; AOTF – Acousto-Optical Tunable Filter).

3. Tissue-like phantom

In order to quantify the performance of the setup, the lateral resolution and the depth sensitivity, a liquid tissue-like phantom with an absorbing inclusion inside was investigated. The inclusion could be linearly moved within the phantom, by means of a programmable XZ-stage (OWIS, Germany), at different depths, to simulate a scanning operational mode. The phantom was prepared using calibrated Intralipid as scatterer and Indian ink as absorber, in such a way to have the following background optical properties: $\mu_a = 0.1$ cm^{-1}, $\mu'_s = 10$ cm^{-1} [17]. For the absorbing inclusion a black PVC cylinder, $\varnothing 6$ mm and 6 mm high, has been used. Despite the nearly total absorption of black PVC, it was demonstrated by Monte Carlo simulations that this kind of phantom provides realistic optical perturbations. In particular, the PVC cylinder yields a perturbation of the DTOF quite close to a 1 cm^3 sphere with an increase in absorption of $\Delta\mu_a = 0.1$ cm^{-1} with respect to the background [18].

4. Measurement procedure

A series of X-scans across the inclusion were recorded by moving the PVC cylinder within the liquid homogeneous phantom at various depths beneath the source/detector point, in order to estimate lateral resolution and depth sensitivity of our system. In practice the centre of the inclusions top surface was aligned with the incident beam at X = 0 and leveled to the surface of the liquid phantom (Z = 0 position). Lateral scanning operation was then simulated by moving the inclusion in steps of 2 mm from X = −30 mm to the X = +30 mm position. X-scans were performed at different depth positions, *i.e.* from Z = 0 to Z = 30 mm in Z steps of 5

mm. In addition, a direct Z-scan from Z = 0 to Z = 30 mm was performed at fixed lateral position X = 0 with smaller steps of 2 mm.
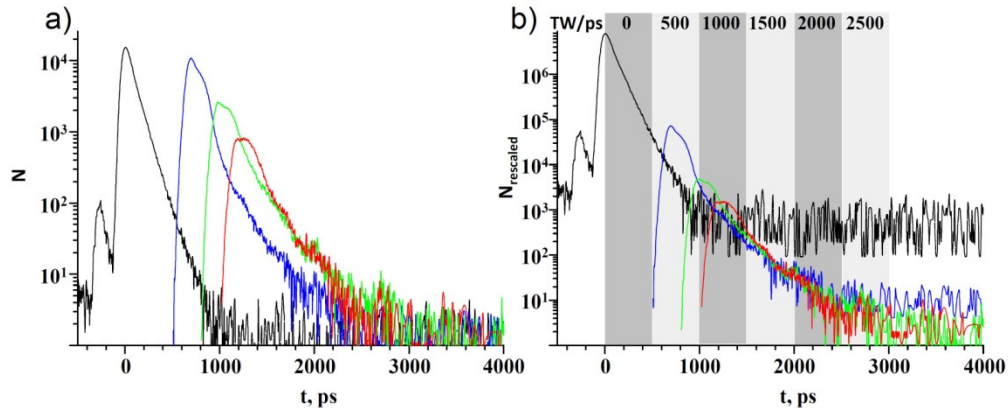

Fig. 2. DTOFs recorded at different gate delays: black curve – full DTOF; blue, green and red curves – DTOFs recorded at gate delays of 1500 ps, 1750 ps and 2000 ps, respectively. (a) DTOFs as originally recorded, (b) DTOFs rescaled with respect to laser power incident to the sample.

The measurements were performed in the following fashion: the inclusion was moved to the next X-, Z-position, then DTOFs at nine different gate delays were acquired. The gating of the fast-gated SPAD was realized with a constant gate width of 6 ns with the gate delay varied from 0 to 2000 ps in steps of 250 ps (relative to the initial gate which allows to record the full DTOF). The collection time of DTOFs was fixed to1 s and the count rate to 500 kHz. Examples of acquired DTOFs are shown in Fig. 2a for an early gate delay allowing to record the full DTOF and the three latest gate delays. For each gate delay at each position of the inclusion a total of 5 DTOFs was acquired and cumulated to increase the signal-to-noise ratio. An almost constant count rate was maintained by adjusting a programmable circular variable attenuator, i.e. the incident power was increased with increasing gate delay. For each gate delay the angular position of the attenuator was recorded, as well as the related current laser power measured by a photodiode.

The data analysis was performed in MATLAB. The five DTOFs recorded for each gate delay of each X-, Z- position were added and baseline corrected (Fig. 2a), and then the amplitudes of the DTOFs were rescaled, taking into account fluctuations and attenuation of the laser power for each particular measurement (see Fig. 2b). Subsequently, the time windows analysis was performed as described in the next Section. Note that the low noise before the leading edge of the gate delayed curves is not visible in the logarithmic representation of the data.

The use of the fast-gated SPAD, insensitive to the initial high photon flux, allowed us to detect very late photons (t > 1000 ps) with a high signal-to-noise ratio (>100). This is illustrated by Fig. 2b: blue, green and red curves are DTOFs recorded at late gate delays with increasing incident power, while the black curve is the full DTOF recorded with low incident power at the first gate delay.

5. Results

The contrast for all X- and Z-scans was calculated, as the figure of merit for the performance assessment of the examined NIRS instrument. The relative contrast C is calculated employing an analysis based on time windows (TWs) as follows:

$$C_i\left(t_g\right) = \frac{N_{i,0}\left(t_g\right) - N_i\left(t_g\right)}{N_{i,0}\left(t_g\right)} \qquad (1)$$

where $N_i(t_g)$ and $N_{i,0}(t_g)$ are the photon counts in the ith TW for the phantom with and without inclusion, respectively, when the gate delay t_g is considered. The beginning of the first TW was set to the peak position of the full DTOF, and the TWs width was set to 500 ps. In Fig. 2b, the TWs considered are shown in alternating shades of grey. The temporal position of each TW is characterized by its starting time. The results obtained for the contrast are presented in Fig. 3a for the X scans and in Fig. 3b for the Z scans.

The columns in both panels represent the different time windows. The rows in Fig. 3a display the X-scans at depths from 0 to 20 mm. The colors of contrast curves in Fig. 3 correspond to the different gate delays as illustrated in Fig. 2. In Fig. 3 no contrast curves are displayed for TW =0 ps, and for TW = 500 ps for the gate delay of 2000 ps, because of the absence of a signal in these time windows prior to gate opening, as can be seen from Fig. 2. The contrast for X-scans (see Fig. 3a) shows the following features. For the shallowest position of the inclusion, Z = 0, i.e. with the upper surface of the cylinder just beneath the surface of the phantom, the maximum relative contrast is 1 at X = 0 for TWs at 500 ps to 2500 ps. That means the count rate virtually drops to zero when source and detector area are exactly above the cylinder. With increasing Z, contrast decreases at all TWs. For TW at 500 ps there is no noticeable contrast at Z = 10 mm and deeper, i.e. photons within this interval of time of flight cannot reach the inclusion. At later TWs, sensitivity to the inclusion appears. For TWs at 1500 ps and later the inclusion is even detectable at 20 mm depth. Upon increasing depth the width of the X-dependent contrast curves increases, i.e. lateral spatial resolution becomes worse, a behavior predicted by MC simulations [10]. When comparing the contrast curves in each row in Fig. 3a, a maximum with respect to time window can be observed, that appears the later the deeper the position of the inclusion is. The results of the Z scans (see Fig. 3b) agree with a comparison of the contrast at X = 0 for each column in Fig. 3a. The maximum contrast drops with depth. However, for later time windows this drop is less steep, and a remarkable contrast is still observed at greater depths.

The results obtained for the three different gate delays in Fig. 3 provide essentially the same contrast values as it is expected from a fast-gated detector whose effect on the measured signal is negligible. However, due to the increasing number of late photons detected at late gate delays, the signal-to-noise ratio depends on gate delay. This effect becomes particularly clear if one observes the high level of noise affecting the contrast for the earliest gate delay analyzed, i.e. for t_g = 1500 ps (blue curves in Figs. 2 and 3).

Unlike for X-scans, 10 DTOFs were acquired at each position of the inclusion and for each gate delay for the Z-scan. Thus, the measurement noise could be estimated by calculating contrast for each out of ten DTOFs and then calculating the mean contrast value and the standard deviation (SD). From an inspection of Fig. 4, it is worth to notice that contrast for the gate delay of 2000 ps has less noise than for the gate delay of 1500 ps, which is a result of a better signal-to-noise ratio of the former one (see Fig. 2b). Furthermore, the noise of the contrast calculated for the TW at 2000 ps is higher than that for TW at 1000 ps for both gate delays. This also follows from Fig. 2b, as a late TW samples more noisy parts of DTOFs. From Fig. 4 one can also determine the depth sensitivity of our non-contact imaging setup. If we define the depth sensitivity as the value of contrast $\sqrt{2}$ times higher than the corresponding SD, in order to distinguish near zero contrast from the noise, it follows that for the gate delay of 1500 ps depth sensitivity is 16 mm and 14 mm for TW at 1000 ps and at 2000 ps respectively, while for the gate delay of 2000 ps depth sensitivity is about 16 mm and 18 mm for TW at 1000 ps and at 2000 ps respectively.
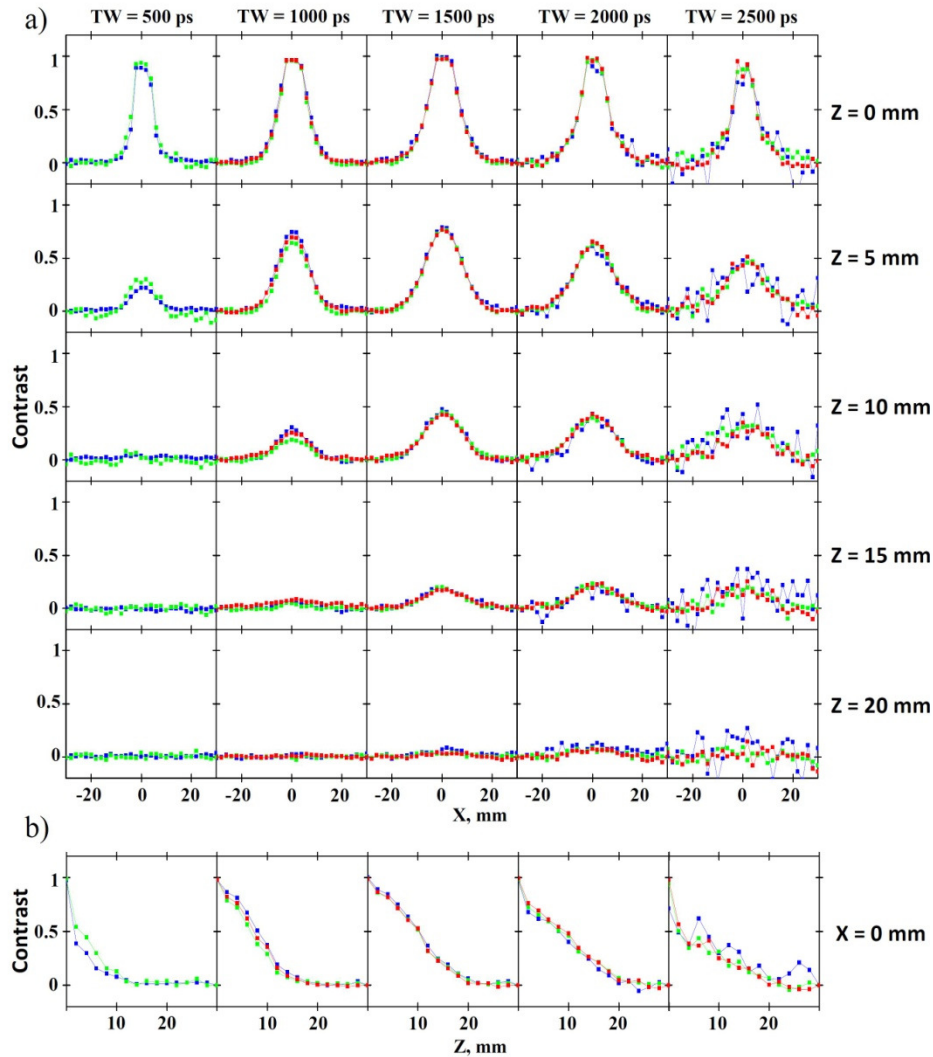
Fig. 3. Contrast for X scans (a) and Z scans (b) of the black cylindrical inclusion for six consecutive time windows of 500 ps (columns). Colors represent the various gate delays, with the same assignment as in Fig. 2. The rows in (a) correspond to different Z positions of the inclusion.

Finally, we compared the contrasts obtained from the measurements with values expected theoretically from a totally absorbing perturbation within an otherwise homogeneous diffusive medium. For this purpose, we performed time-resolved Monte Carlo simulations reproducing the same optical properties and geometry of the experiment and convolved them with the measured instrument response function. Contrasts calculated from MC simulations for a source-detector separation of 2 mm are shown in Fig. 4 as black lines. These findings are in substantial agreement with the experimental results.
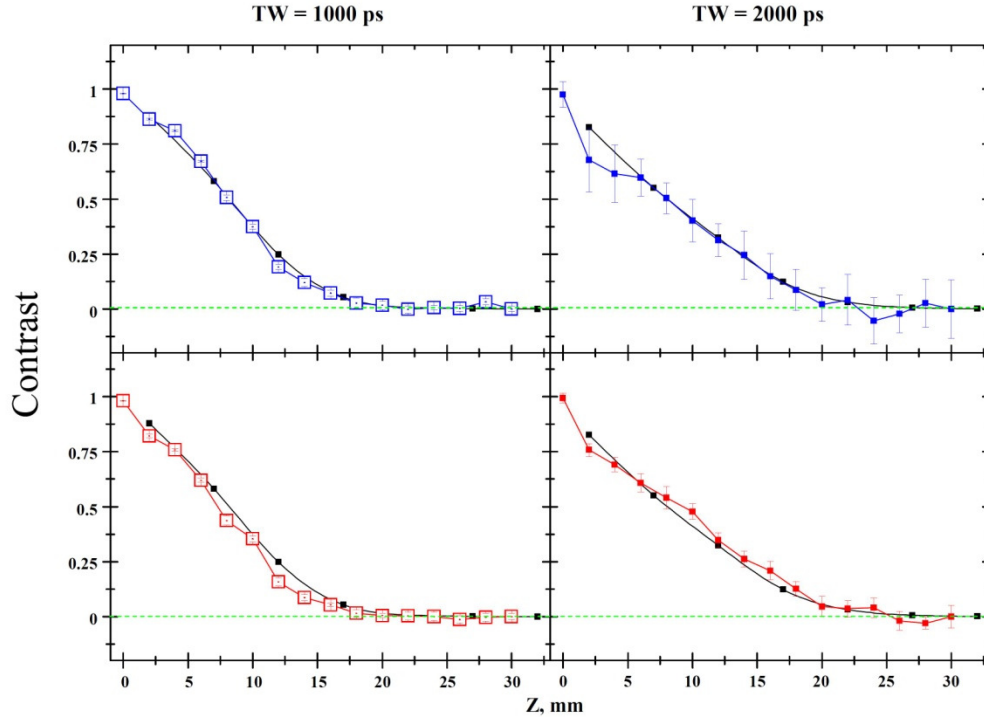
Fig. 4. Comparison of the experimental data with MC simulations for time-resolved contrasts due to a totally absorbing perturbation in an otherwise homogeneous diffusive medium, for 2 mm source-detector separation. Here are reported Z-scans for TWs at 1000 (left) and 2000 ps (right), for gate delays of 1500 (up, blue line) and 2000 ps (down, red line). MC simulations are represented by black lines.

6. Conclusion

We have demonstrated the feasibility of non-contact diffuse optical imaging, exploiting the null source-detector separation approach using a fast-gated SPAD detector. Measurements on a tissue-like phantom with a buried local inhomogeneity showed depth sensitivity down to about 2 cm and a lateral resolution comparable with that of fiber-based contact approach. The development of a scanning prototype for in-vivo measurements is in progress. Applications are envisaged in the area of functional brain imaging, brain injury detection, optical mammography, imaging of joint inflammation. The non-contact nature of the imaging system can help solving problems of the sensor-tissue contact, will be more comfortable for subjects, may allow to track untethered movement of head or limbs.

Acknowledgments